Human-induced changes to the global ocean water-masses and their time of emergence

Yona Silvy, Éric Guilyardi, Jean-Baptiste Sallée, Paul J. Durack

Human-induced changes to the global ocean water-masses and their time of emergence

Yona Silvy[1,*], Eric Guilyardi[1,2], Jean-Baptiste Sallée[1] and Paul J. Durack[3]

[1]*LOCEAN-IPSL, Laboratoire d'Océanographie et du Climat : Expérimentation et Approches Numériques (Sorbonne Université/CNRS/IRD/MNHN), Paris, France*

[2]*NCAS-Climate, University of Reading, UK*

[3]*Program for Climate Model Diagnosis and Intercomparison, Lawrence Livermore National Laboratory, Livermore, California, USA*

Corresponding author:

Yona Silvy (yona.silvy@locean-ipsl.upmc.fr)

LOCEAN-IPSL

Sorbonne Université, Boîte 100, 4 place Jussieu, 75252 Paris

[Abstract]

The World Ocean is rapidly changing, with global and regional modification of temperature and salinity, resulting in widespread and irreversible impacts. While the most pronounced observed temperature and salinity changes are located in the upper ocean, changes in water-masses at depth have been identified and will likely strengthen in the future. Here, using 11 climate models, we define when anthropogenic temperature and salinity changes are expected to emerge from natural variability in the ocean interior along density surfaces. The models predict that in 2020, 20–55% of the Atlantic, Pacific and Indian basins have an emergent anthropogenic signal; reaching 40–65% in 2050, and 55–80% in 2080. The well-ventilated Southern Ocean water-masses emerge very rapidly, as early as the 1980s-1990s, while the Northern Hemisphere emerges in the 2010s-2030s. Our results highlight the importance of maintaining and augmenting an ocean observing system capable of detecting and monitoring persistent anthropogenic changes.

[Main]

Observed ocean temperature and salinity changes have been partially attributed to human activities, with global ocean heat content change identified in the early 2000s[1,2], and temperature and salinity changes in the upper (0-700 m) and intermediate (700-2000 m) ocean in more recent times[3–11]. A few studies focused on more specific regions, with detected human-induced changes to ocean salinity in the Tropical Pacific[9], the Atlantic[10], and the Southern Ocean[11]. However, there are still vast regions of the World Ocean, particularly at depth, where anthropogenic change remains undetected. The lack of positive attribution can be due to poor observational coverage, weak changes, or because natural variability is large and is hiding forced changes. Because of the slow transport of heat and salt in the ocean interior, some regions in the deep ocean may be isolated from human-induced changes for a long time as the climate signal propagates from the surface to the ocean interior. Other regions, which are more directly connected to the surface by atmosphere-ocean exchanges, ocean circulation and mixing, may respond more quickly. Based on anthropogenically-forced climate model simulations it is possible to estimate where and when the human-induced signal emerges against the natural background climate variability in the ocean interior.

While investigating the timescale of anthropogenic signal emergence in the climate system, past studies have focused on surface temperature[12–17], precipitation[18,19], sea level rise[20] as well as marine ecosystem drivers and ocean carbon cycle indicators[21–26]. It was shown that temperature and salinity are potentially good indicators for detecting anthropogenic change in the next few decades[27]. Here, we investigate for the first time the emergence and associated probabilistic range of human-induced salinity changes at depth, in basin-scale zonal means, using a multi-model framework. We

focus on the ocean interior below the "bowl", i.e. below the deepest winter mixed layer and we use climate models participating in the 5th phase of the coupled model intercomparison project (CMIP5). Ocean circulation below the bowl primarily flows along density surfaces. Density surfaces can move vertically (heave) for several reasons including transient dynamical changes unrelated to atmosphere-forced and ocean-ingested heat or freshwater changes, that manifest as temperature and salinity changes when assessed on a given pressure level. In an endeavour to detect the earliest time of emergence, we therefore remove from our analysis all signal associated to transient dynamical change by investigating temperature and salinity changes on neutral density levels (see Methods). On a density surface, changes of salinity and temperature are by definition correlated, so to avoid redundancy we will hereafter only discuss salinity changes.

Observed zonally-averaged salinity changes along density surfaces show remarkably similar structures across different basins in the Southern Hemisphere (Figure 1a, Supplementary Figure 1a)[28,29]. These features include a subtropical freshening in the upper 1000 metres in the density range of Subantarctic Mode and Intermediate Waters (26.5-27 $kg.m^{-3}$), surrounded by a relatively strong salinity increase in the tropical shallow cells and a slightly more moderate salinity increase in the range of Upper Circumpolar Deep Waters (~50ºS-60ºS, ~27.5 $kg.m^{-3}$). The Northern Hemisphere Pacific presents a similar geographical salinification/freshening/salinification pattern of change. The North Atlantic features a subpolar freshening extending into the subtropics along the 27.7-28 $kg.m^{-3}$ isopycnals as well as a freshening along the 27 $kg.m^{-3}$ isopycnal from the subtropics to the equator and southward, capped by a strong salinity increase in the upper ocean and smaller increase at depth. Strong salinification

is observed in the North Indian, spanning almost all density ranges and suggesting the influence of marginal sea outflows of high salinity dominates.

These large-scale patterns of multi-decadal change have been proposed to be caused by regional surface changes in freshwater fluxes[29–32] (wet regions get wetter and dry regions get dryer), as well as from surface warming shifting isopycnal outcrops poleward and along which the signal penetrates the ocean interior[30–32].

Although the amplitude of the change is weaker in the multi-model mean (MMM of 11 models; Figure 1b and Supplementary Figure 1b) than in the observation-based estimate – which is expected for a multi-model ensemble mean as it washes out change patterns of water-masses with slightly different geographies thus not exactly aligned – the main patterns of change are reproduced. Indeed, the observed salinification/freshening/salinification from equator to pole in the Southern Hemisphere of all three basins and in the Northern Hemisphere Pacific is replicated in the models, although we note the Mode Water freshening in the Southern Hemisphere tends to appear on slightly lighter density classes in the models than in the observations (around 26 $kg.m^{-3}$ in the models versus 26.5-27 $kg.m^{-3}$ in the observations), consistent with past studies[11,31,33]. The magnitude of change within the individual model ensembles is equivalent to observed estimates (Supplementary Figure 3) and the change is robust across models in regions where the observed signal is the strongest, indicative of a coherent forced change. The Northern Indian ocean shows a change pattern of opposite sign in the MMM than in observations, as models have large regional errors there. As the Durack & Wijffels 2010 (hereafter DW10) analysis ends in 2008 (Figure 1a), we also compute the 1950-2017 change using the EN4[34] observation-based ocean reanalysis (Supplementary Figure 2a). The EN4 spatial

patterns of change are extremely similar to those of DW10, giving confidence in the robustness of these identified observed patterns. In the MMM, the patterns of change identified during the 1950-2008 period (Figure 1b and Supplementary Figure 1b) become more robust when extending the period to 2017 and the amplitude of the change increases (Supplementary Figure 2b).

To more quantitatively compare the observed and simulated trends in water-masses regionally, a diagnostic of the trends in 9 regions of interest is shown (Figure 1c). In both observations and models, these regions correspond to the salinity increase in the subpolar Southern Ocean, the freshening in the Southern Hemisphere subtropics, the increase (freshening) in the northern subtropical Atlantic (Pacific) and the increase in the subpolar North Pacific. The coordinates are chosen to best capture these patterns and tailored to the water-mass ranges of each model as those are not necessarily reproduced at the same locations. Approximate boxes are shown in Figure 1a, and the exact boxes can be found in Supplementary Figure 1a for the observations and Supplementary Figure 4 for each model. We also run the same diagnostic for EN4. Regional trends in the observational estimates and models (Figure 1c) are within the same order of magnitude, although the DW10 values tend to lie systematically on the higher end of the model distribution or even outside in some sections of the poorly-sampled Southern Hemisphere, suggesting that the models might simulate a conservative estimate of the change. In the well-sampled Northern Hemisphere, both observational estimates fall within the model distribution. In all regions, EN4 yields a smaller trend than DW10, consistent with the respective methods of these estimates (in data-sparse regions, EN4 is restored towards the climatology, thus providing a very conservative estimate of change). Overall, this gives us confidence in the ability of models to reproduce these regional patterns of change.

Based on the same model suite, we now determine the "anthropogenic" component of the change by subtracting from the salinity computed in the historical simulations, the salinity computed in idealized coincident simulations where human-induced forcings are removed (historicalNat). At the end of the 20th century it is striking that the simulated historical change (Figure 1b) is very close to the estimated "anthropogenic" contribution (Figure 2a), with a Pearson's spatial correlation coefficient of 0.88, suggesting that human-induced forcings are responsible for most of the observed salinity change during the 2nd half of the 20th century[5,9–11]. The pattern of the historical anthropogenic signal is further amplified from 2006 and into the 21st century under a high emission scenario (RCP8.5; Figure 2b), confirming the robustness of the structures of the anthropogenic forced change over the observed time period. As this signal appears qualitatively robust and human-induced, we now investigate when it can be statistically unambiguously distinguished from natural background variability over the 1861-2100 period (note that unlike previous studies, we use "natural" rather than "unforced" variability, see Methods).

We define the time of emergence (ToE) of salinity change as the year when the anthropogenic signal (ranging from 1861 to 2100) exceeds and never falls back below twice the typical natural variability "noise" threshold (the interannual standard deviation of the historicalNat experiment), such that emergence is detected within the 95% confidence interval (see Methods for details). We are choosing a rather high estimate of the noise envelope (see Methods), thus possibly yielding conservative ToE results. Nevertheless, early detection is found: in all regions that show a robust pattern of change, the multi-model median ToE falls between the late 20th century and the first

decades of the 21st century (Figure 3a) and there is a noteworthy agreement between models on the sign of the signal (see also inter-model spread in Supplementary Figure 5). Regions that do not emerge show no agreement between models (grey areas in Figure 3a). In 2020, most of the identified forced patterns have already emerged in the ocean interior, with 20-45% of the zonally averaged basin emerged in the Atlantic; 20-55% in the Pacific and 25-50% in the Indian (Figure 3b, 1st-3rd quartiles). These numbers rapidly increase, reaching 35-55% in the Atlantic in 2050 to 55-65% in 2080; 45-65% to 60-75% in the Pacific; 45-65% to 60-80% in the Indian.

The earliest ToE are found in the Southern Hemisphere subtropical (40-20ºS) and subpolar (60-40ºS) areas, with a median ToE as early as the 1980s, and overall earlier than 2020. The subtropical Southern Ocean is a dominant region for heat uptake associated with the formation and subduction of water-masses ventilating the subtropical gyres with Mode and Intermediate waters[33,35]. The early emergence of the human-induced signal in this region is consistent with the observed changes that have been detected and attributed to anthropogenic forcings[11]. Model agreement in the southern subtropical Atlantic from 40–20°S is weak in the upper 1000 m, reflecting that unlike the Indian and Pacific, this basin is not associated with a well ventilated layer of Subantarctic Mode water[35]. Instead, the upper 1000 m in the Southern Ocean Atlantic basin is populated with newly ventilated Intermediate waters[35], whose circulation and subduction are poorly represented by the CMIP5 model suite[33]. The model spread is relatively narrow for the Southern Hemisphere subtropics (2-3 decades for the interquartile range in the Pacific and Indian sectors; Supplementary Figure 5), and slightly larger for the subpolar Southern Ocean. We note that the emergence in the subpolar Southern Ocean is to be assessed cautiously, with most models rapidly

limiting spurious open ocean deep convection due to near-surface freshening[36,37], therefore arguably warming at depth (1000-2000 m) much faster than in the real world (in the subpolar Southern Ocean, deep convection acts to extract heat from the interior ocean and release it to the atmosphere[38]). The other regions featuring an emergence of the signal in the first decades of the 21st century are the northern Pacific between 10-30°N and 40°N-60°N, with a median ToE from the 2010s to 2040 and an inter-model range of a few decades. The signal in the North Atlantic also emerges in the early decades of the 21st century, mostly before 2020, with an interquartile range of two to four decades. The inter-model range gives a measure of the uncertainty that the climate models are providing, and so a spectrum of possibilities for the real world to lie within. There is decadal to multi-decadal variability between realizations and between models, as well as model errors, which means it is difficult to get that range below O(10 years).

Because each model can represent a given water-mass at slightly different latitude or density, we again delineate model-specific water-mass ranges that are uniquely defined for each model, so a clearer, quantitative water-mass centric model intercomparison can be performed (same regions as Figure 1c; see approximate regions in Figure 2b and exact boxes for each model in Supplementary Figure 4 in original density space). Additionally, and again to increase the signal to noise ratio, because each model can have a different climate sensitivity for a given forcing scenario, here we associate, for each model member, the ToE of the anthropogenic signal in all 9 regions to the corresponding global mean surface warming at that time under the RCP8.5 scenario (global mean surface air temperature (GSAT) increase relative to the pre-industrial era, Figure 4). Supplementary Figure 6 shows the same analysis, as a function of time (ToE axis instead of GSAT anomaly).

Most models predict that salinity change signals emerge between +0.5ºC and +2ºC of global mean surface warming, corresponding to a ToE between the late 20th century and the first decades of the 21st century (Figure 4). According to this distribution, there is a 100% probability for the anthropogenic signal in the Northern subpolar Pacific and in the Southern Hemisphere Pacific and Indian subtropics to emerge before a +2ºC warming, and over 75% probability to emerge before +1.5ºC – and even before +1ºC for the Pacific southern subtropics (note observed global mean surface warming to 2018 is about 1ºC[39]). The subpolar Southern Ocean sectors have a relatively early median emergence (~0.8ºC-1.3ºC), but a wide model spread, especially in the Pacific, probably reflecting model deficiencies in representing this part of the ocean[36,37]. The Northern Hemisphere subtropical water-masses emerge slightly later than their Southern Hemisphere counterparts (except in the Atlantic basin), with about 75% probability to emerge before +2.25°C. We expect the dependence of these results to slower warming scenarios (different RCPs) to be limited, as most models present a signal emerging before there is a significant difference between scenarios (see comparison of the RCP4.5 and RCP8.5 warming in Supplementary Figure 7).

We repeat the same analysis on an idealized emission scenario where CO2 concentration in the atmosphere increases by 1% every year (1pctCO2), i.e. a much faster forcing than observed in the 20th century or projected for the 21st century (see Supplementary Figures 6 and 8, and CO2 signal patterns in Supplementary Figure 9). The overall agreement in the emergence of a climate signal in different water-masses across the different models and the two types of very different timing of forcing scenarios (RCP8.5, 1pctCO2) offers confidence in simulated emergence patterns and confirms the dominant role of CO2 emissions.

In analysing emergence timescales in the climate system, previous studies[20,21] showed that spatial patterns of ToE are strongly determined by the unforced variability, meaning that an earlier ToE arises in regions of weaker noise and vice-versa. We investigate whether this is the case by examining the relative contributions of signal and noise to the ToE regional pattern for each model, as well as the regional inter-model spread (see Supplementary Discussion and Supplementary Figures 12 and 13). We find that the time-independent noise level is not sufficient to explain the ToE spread, which seems predominantly explained by the signal across regions and models, i.e. either its strength, or its decadal to multi-decadal variability. This suggests that the low noise level of the ocean interior makes it a unique place for early detection of human-induced changes, even with the conservative estimate used here. Indeed, although the anthropogenic climate signal might appear at the surface first, strong background variability there can delay its emergence and counter-intuitively earlier emergence can be found in the ocean interior, with geographical differences compared to the surface. Surface air temperature and sea surface temperature in the RCP8.5 scenario were found to emerge mainly within the early to mid 21st century, showing strong regional differences with earlier emergence in the tropics due to the low noise level there than at higher latitudes[14,15,20]. ToE is especially late in the Southern Ocean for surface temperature, whereas we find the earliest emergence in this part of the world under the surface. Half of the ocean area is expected to have emergent thermosteric sea level rise in the 2040s, and when including additional effects such as ice mass loss, as early as 2020[20]. It is interesting to see that the timing of emergence of changing patterns occurs differently for different variables, probably a testimony of their distinctive interactions and feedbacks in the Earth system. This is clearly

illustrated by the very different patterns and timing of emergence of the change in the different components of the ocean carbon cycle[26]. The diversity of climate variables investigated collectively provides a comprehensive understanding of the time of emergence of the human-induced change in the Earth System, into which this study is contributing additional insight.

This work suggests that a large portion of the observed change patterns in the ocean interior is human-induced and will continue to respond to CO2 emissions. If these patterns have been suggested to be primarily driven by an increased surface warming and water-cycle amplification[29,31] (two processes that directly affect heat and salt in the ocean thus density and circulation), understanding how these patterns will continue to amplify in the future in a more stratified upper ocean[40] and with possibly modified ocean circulation and mixing requires further investigation. In particular deciphering which of the changing surface fluxes is likely to play a larger role, where and on what timescales, can be for example explored with model-specific FAFMIP-like[41,42] mechanistic studies.

The Hemispheric asymmetry in emergence, with earlier ToEs in the Southern Hemisphere subtropics is reminiscent of a number of recent studies stressing the importance of the Southern Ocean for ocean heat and carbon storage, associated with the overturning circulation[43–45]. It is noteworthy that this part of the world is historically the most poorly sampled, and therefore the worst positioned for detecting a forced climate signal in observations[46,47]. The global pattern of human-induced fingerprint of ocean interior change can be used to guide the future development of a targeted global ocean observing system focused at monitoring and detecting future ocean change. The maintenance of this observing system along with continued

investment in climate and ocean model development and evaluation, will provide the necessary measurements and model tools to best inform adaptation and mitigation strategies and policies going forward.

[Methods]

Density binning of CMIP5 simulations

In this study, we use a suite of CMIP5 climate models binned into a neutral density framework, using the McDougall and Jackett (2005)[48] routine, to examine anthropogenic signal in the ocean on approximated neutral surfaces (γ^a) compared with natural climate variability. Zonal means are computed for each oceanic basin along neutral density surfaces, which allows for a more water mass-centric assessment than is possible using a standard pressure level analysis. We note that some vertical movement (heave) of density surfaces can be due to climate change[49,50], but we don't investigate those here. In addition to providing a cleaner signal and reducing the noise, the density framework provides several other benefits, including a view of the ocean interior delineated by its water-masses, useful for intermodel comparison[33,51], as water-masses can be defined by their density range. Additionally, along density surfaces, salinity and temperature changes compensate and thus have the same structure and sign, and consequently the same emergence timescale.

To allow for a simpler and more intuitive visual representation, zonally-averaged values are then remapped back to a pseudo-depth coordinate using a γ^a to pressure relationship derived from observation-based product EN4[34] by a surface-to-bottom mapping of the ocean per density layer. Note that all remapping of this paper, irrespective of whether we are in the context of past, contemporary, or future, is done

with the exact same γ^a to pressure relationship which is based on contemporary observations. The remapping is purely a visual tool here, which does not introduce any signal: all signal, noise and ToE computations are done in γ^a space. All the data is trimmed at the bowl (i.e. below the winter mixed layer depth), indicated by a dark grey shading in the figures.

ToE definition

The ToE is computed both locally (for each grid point; Figure 3) and regionally in a number of determined regions, using a manual fingerprint (i.e. regional model-specific boxes fixed in time) to track the signal (Figure 4). We use an ensemble of 11 models with a total of 35 realizations for the anthropogenic ToE, and 13 single-member models for the CO_2 ToE (see Supplementary Table 1). The ToE is computed for each individual member, then inter-member medians are derived, yielding a multi-model distribution with the same weight for each model, and thus an estimate of the uncertainty.

The anthropogenic signal is 240 years long, ranging from 1861 to 2100. It is defined over the historical period (1861-2005) at each yearly time step as the salinity difference between the historical experiment (fully-forced) and the time averaged historicalNat value (natural forcings only: solar fluctuations and volcanic eruptions); and defined over the projection period (2006-2100) at each yearly time step by the salinity change between the RCP8.5 scenario ("business as usual") and the time averaged historicalNat value (same baseline for both periods to insure continuity). For each historical+RCP8.5 ensemble member, the historicalNat time series used as the baseline of the signal is the ensemble mean.

We note that the correct term for the signal defined above should be "externally forced" as the influence of external natural forcings can be present during the historical period; however, considering the greater influence of human-induced forcings over time and especially in the ocean interior, we therefore refer to this signal as "anthropogenic". The possible influence of external natural forcings in the signal during the historical period will occur in terms of additional decadal to multidecadal variability.

The noise represents the bounds of background climate variability, and is built from the interannual standard deviation of the historicalNat experiment (1861-2005, over 145 years). Within several historical+RCP8.5 members of a model, the noise is the same and is defined using the maximum standard deviation of all available historicalNat realizations within that model. The threshold of signal exceedance over noise is chosen at two based on the large consensus in existing literature, and because it represents a 95% confidence of signal emergence, but sensitivity to this threshold is discussed in the Supplementary Materials (see Supplementary Figure 10). Overall, this definition makes it a rather high (thus conservative) estimate of the noise envelope (interannual noise, historicalNat choice instead of a pre-industrial control, two standard deviations as the threshold and picking the maximum among historicalNat members). The signal is considered to have emerged if it definitively exceeds the noise threshold at least 20 years before the end of the projection to account for potential "false" emergence - i.e. if the signal were to go back within the bounds of climate variability afterwards[20,52]. Note that some internal variability (and natural variability over the historical period due to volcanic and sun forcings) remains in our signal definition, which is not exactly the purely forced response to anthropogenic forcings

such as can be identified with the multi-model mean of a large ensemble, but is rather a change and thus more similar to what real observational time series would look like. The historicalNat experiment is a coherent choice for estimating natural climate variability as it accounts for internal variability as well as external natural forcings, both included in the forced experiments. However, we do test how our results are affected by using the pre-industrial control (no external forcings) instead of the historicalNat experiment in defining the noise, as is often done, and do not find the time of emergence distributions to be much altered (see Supplementary Figure 11). The change driven by the CO2 forcing alone can be estimated in a similar way, by taking the salinity difference between the yearly idealized 1pctCO2 experiment (140 years) and the mean value of the pre-industrial control. The noise for CO2 ToE is then defined as the standard deviation of the pre-industrial control over the last 240 years (as to have the same noise definition as done in Supplementary Figure 11 for the turquoise boxes).

ToE distribution of basin zonal means

The gridpoint-per-gridpoint ToE distribution is calculated based on Lyu et al.'s (2014)[20] methodology. A signal is considered to have emerged if its ToE is at least 20 years earlier than the end of the time series (2080 for the RCP8.5, 120 for the 1pctCO2). At each gridpoint, the signal of each model realization can emerge with either a positive (salinity increase) or negative (freshening) change, or not emerge at all and stay within the bounds of climate variability. The distribution can be calculated if at least half of the runs emerge with the same sign of the signal, or at least half of the runs show no emergence, and if the outliers that have a different direction of change are less than 5 (5 for the anthropogenic signal, 1 for the pure CO2). We then compute

the distribution by excluding the outliers, first by computing the inter-member medians, then the multi-model distribution using these medians so as to give each model the same weight. If the conditions are not met, the location is labelled as "no agreement". See Lyu et al. (2014) supplementary material for details and examples.

Manual fingerprint

The regional ToEs are calculated by averaging both signal and noise in selected regions (see Figure 2b). Namely, we defined: the Southern Ocean subpolar range, encompassing signal associated with Upper Circumpolar Deep Water (around 40–60°S; 27-28 kg.m-3); the Southern Ocean subtropical range, encompassing signal associated with Mode and Intermediate Waters (around 20–40°S; 25-26.5 kg.m-3); the Northern Hemisphere subtropical range, encompassing signal associated with Atlantic and Pacific Mode Waters (around 20–40°N; 25-26 kg.m-3 in the Pacific; 26-27 kg.m-3 in the Atlantic), and the Subpolar North Pacific, encompassing signal associated with the North Pacific Intermediate Waters (around 40-60°N; 26-27 kg.m-3). The boxed coordinates are model-specific, and were fixed (in γ^a space) based on the zonally-averaged spatial pattern of the signal at the end of the time series (see Supplementary Figure 4). The regional emergence of the signal (Figure 4) is based on a manual fingerprint for each region displayed, thus slightly sensitive to the precise boxes used. The patterns of change that already exist in the historical forced simulations continue to exist in the same locations and enhance in the 21st century simulations, giving us confidence in using boxes fixed in time.

Warming scale

Global surface warming at emergence was computed by taking each run's GSAT (historical+RCP8.5) smoothed with a 10-year running mean, at the time of emergence in each region. GSAT anomaly is calculated relative to the 1850-1900 period. The same was done for the 1pctCO2 GSAT (Supplementary Figure 8).

Percentage of basin emergence

We define the percentage of emerged area in basin zonal means and under the surface bowl at each time step by computing the cumulative sum over each basin of the number of grid cells that have emerged before that time step, weighted by the thickness of their respective density layer; and dividing it by the cumulative sum of each grid cell's isopycnal thickness of that same basin zonal mean. The result is given in terms of area as the latitudinal grid is regular with a 1° resolution (all models were interpolated on that same horizontal regular grid). This is done for every model simulation, then the inter-member medians are computed. Shown in Figure 3b are the median, 1st and 3rd quartiles of the multi-model distribution.

[Acknowledgments]

We wish to thank Casimir de Lavergne, Alexey Fedorov, Peter Gleckler, Jonathan Gregory, Ed Hawkins, Gurvan Madec, Herlé Mercier, Juliette Mignot, Ben Santer and Laurent Terray for helpful discussions. We acknowledge the support from the "Make Our Planet Great Again" project ARCHANGE (Agence Nationale pour la Recherche project ANR-18-MPGA-0001), from the European Research Council (ERC) under the European Union's Horizon 2020 research and innovation program (grant agreement 637770) and from the Centre National de la Recherche Scientifique. We also acknowledge the CMIP5 modelling groups, the ESGF and IPSL/ESPRI-MOD data distribution systems. The work of PJD was prepared by Lawrence Livermore National Laboratory (LLNL) under Contract DE-AC52-07NA27344 and is a contribution to the U.S. Department of Energy, Office of Science, Climate and Environmental Sciences Division, Regional and Global Modeling and Analysis Program. LLNL Release number: LLNL-JRNL-794900.

[References]

1. Barnett, T. P., Pierce, D. W. & Schnur, R. Detection of Anthropogenic Climate Change in the World's Oceans. *Science* **292**, 270–274 (2001).
2. Reichert, B. K., Schnur, R. & Bengtsson, L. Global ocean warming tied to anthropogenic forcing. *Geophys. Res. Lett.* **29**, 20-1-20–4 (2002).
3. Barnett, T. P. *et al.* Penetration of Human-Induced Warming into the World's Oceans. *Science* **309**, 284–287 (2005).
4. Palmer, M. D., Good, S. A., Haines, K., Rayner, N. A. & Stott, P. A. A new perspective on warming of the global oceans. *Geophys. Res. Lett.* **36**, (2009).
5. Pierce, D. W., Gleckler, P. J., Barnett, T. P., Santer, B. D. & Durack, P. J. The fingerprint of human-induced changes in the ocean's salinity and temperature fields. *Geophys. Res. Lett.* **39**, (2012).
6. Gleckler, P. J. *et al.* Human-induced global ocean warming on multidecadal timescales. *Nat. Clim. Change* **2**, 524–529 (2012).
7. Tokarska, K. B., Hegerl, G. C., Schurer, A. P., Ribes, A. & Fasullo, J. T. Quantifying human contributions to past and future ocean warming and thermosteric sea level rise. *Environ. Res. Lett.* **14**, 074020 (2019).
8. Bilbao, R. A. F., Gregory, J. M., Bouttes, N., Palmer, M. D. & Stott, P. Attribution of ocean temperature change to anthropogenic and natural forcings using the temporal, vertical and geographical structure. *Clim. Dyn.* (2019) doi:10.1007/s00382-019-04910-1.
9. Terray, L. *et al.* Near-Surface Salinity as Nature's Rain Gauge to Detect Human Influence on the Tropical Water Cycle. *J. Clim.* **25**, 958–977 (2012).
10. Stott, P. A., Sutton, R. T. & Smith, D. M. Detection and attribution of Atlantic salinity changes. *Geophys. Res. Lett.* **35**, (2008).
11. Swart, N. C., Gille, S. T., Fyfe, J. C. & Gillett, N. P. Recent Southern Ocean warming and freshening driven by greenhouse gas emissions and ozone depletion. *Nat. Geosci.* **11**, 836-+ (2018).
12. Mahlstein, I., Knutti, R., Solomon, S. & Portmann, R. W. Early onset of significant local warming in low latitude countries. *Environ. Res. Lett.* **6**, 034009 (2011).
13. Diffenbaugh, N. S. & Scherer, M. Observational and model evidence of global emergence of permanent, unprecedented heat in the 20th and 21st centuries. *Clim.*

491 *Change* **107**, 615–624 (2011).
492 14. Hawkins, E. & Sutton, R. Time of emergence of climate signals. *Geophys. Res.*
493 *Lett.* **39**, n/a-n/a (2012).
494 15. Mora, C. *et al.* The projected timing of climate departure from recent variability.
495 *Nature* **502**, 183–187 (2013).
496 16. Diffenbaugh, N. S. & Charland, A. Probability of emergence of novel
497 temperature regimes at different levels of cumulative carbon emissions. *Front. Ecol.*
498 *Environ.* **14**, 418–423 (2016).
499 17. Lehner, F., Deser, C. & Terray, L. Toward a New Estimate of "Time of
500 Emergence" of Anthropogenic Warming: Insights from Dynamical Adjustment and a
501 Large Initial-Condition Model Ensemble. *J. Clim.* **30**, 7739–7756 (2017).
502 18. Giorgi, F. & Bi, X. Time of emergence (TOE) of GHG-forced precipitation
503 change hot-spots. *Geophys. Res. Lett.* **36**, (2009).
504 19. Mahlstein, I., Portmann, R. W., Daniel, J. S., Solomon, S. & Knutti, R.
505 Perceptible changes in regional precipitation in a future climate. *Geophys. Res. Lett.* **39**,
506 (2012).
507 20. Lyu, K., Zhang, X., Church, J. A., Slangen, A. B. A. & Hu, J. Time of
508 emergence for regional sea-level change. *Nat. Clim. Change* **4**, (2014).
509 21. Keller, K. M., Joos, F. & Raible, C. C. Time of emergence of trends in ocean
510 biogeochemistry. *Biogeosciences* **11**, 3647–3659 (2014).
511 22. Rodgers, K. B., Lin, J. & Frölicher, T. L. Emergence of multiple ocean
512 ecosystem drivers in a large ensemble suite with an Earth system model. *Biogeosciences*
513 **12**, 3301–3320 (2015).
514 23. Frölicher, T. L., Rodgers, K. B., Stock, C. A. & Cheung, W. W. L. Sources of
515 uncertainties in 21st century projections of potential ocean ecosystem stressors. *Glob.*
516 *Biogeochem. Cycles* **30**, 1224–1243 (2016).
517 24. Henson, S. A. *et al.* Rapid emergence of climate change in environmental
518 drivers of marine ecosystems. *Nat. Commun.* **8**, 14682 (2017).
519 25. Turk, D. *et al.* Time of Emergence of Surface Ocean Carbon Dioxide Trends in
520 the North American Coastal Margins in Support of Ocean Acidification Observing
521 System Design. *Front. Mar. Sci.* **6**, (2019).
522 26. Schlunegger, S. *et al.* Emergence of anthropogenic signals in the ocean carbon
523 cycle. *Nat. Clim. Change* 1–7 (2019) doi:10.1038/s41558-019-0553-2.
524 27. Banks, H. & Wood, R. Where to Look for Anthropogenic Climate Change in the

525 Ocean. *J. Clim.* **15**, 879–891 (2002).
526 28. Helm, K. P., Bindoff, N. L. & Church, J. A. Changes in the global hydrological-
527 cycle inferred from ocean salinity. *Geophys. Res. Lett.* **37**, (2010).
528 29. Durack, P. J. & Wijffels, S. E. Fifty-Year Trends in Global Ocean Salinities and
529 Their Relationship to Broad-Scale Warming. *J. Clim.* **23**, 4342–4362 (2010).
530 30. Durack, P. J., Wijffels, S. E. & Matear, R. J. Ocean Salinities Reveal Strong
531 Global Water Cycle Intensification During 1950 to 2000. *Science* **336**, 455–458 (2012).
532 31. Lago, V. *et al.* Simulating the Role of Surface Forcing on Observed
533 Multidecadal Upper-Ocean Salinity Changes. *J. Clim.* **29**, 5575–5588 (2016).
534 32. Zika, J. D. *et al.* Improved estimates of water cycle change from ocean salinity:
535 the key role of ocean warming. *Environ. Res. Lett.* **13**, 074036 (2018).
536 33. Sallee, J.-B. *et al.* Assessment of Southern Ocean water mass circulation and
537 characteristics in CMIP5 models: Historical bias and forcing response. *J. Geophys.*
538 *Res.-Oceans* **118**, 1830–1844 (2013).
539 34. Good, S. A., Martin, M. J. & Rayner, N. A. EN4: Quality controlled ocean
540 temperature and salinity profiles and monthly objective analyses with uncertainty
541 estimates: THE EN4 DATA SET. *J. Geophys. Res. Oceans* **118**, 6704–6716 (2013).
542 35. Sallée, J.-B., Speer, K., Rintoul, S. & Wijffels, S. Southern Ocean Thermocline
543 Ventilation. *J. Phys. Oceanogr.* **40**, 509–529 (2010).
544 36. de Lavergne, C., Palter, J. B., Galbraith, E. D., Bernardello, R. & Marinov, I.
545 Cessation of deep convection in the open Southern Ocean under anthropogenic climate
546 change. *Nat. Clim. Change* **4**, 278–282 (2014).
547 37. Heuzé, C., Ridley, J. K., Calvert, D., Stevens, D. P. & Heywood, K. J.
548 Increasing vertical mixing to reduce Southern Ocean deep convection in NEMO3.4.
549 *Geosci. Model Dev.* **8**, 3119–3130 (2015).
550 38. Dufour, C. O. *et al.* Preconditioning of the Weddell Sea Polynya by the Ocean
551 Mesoscale and Dense Water Overflows. *J. Clim.* **30**, 7719–7737 (2017).
552 39. Intergovernmental Panel on Climate Change. Summary for Policymakers. in
553 *Global warming of 1.5°C. An IPCC Special Report on the impacts of global warming of*
554 *1.5°C above pre-industrial levels and related global greenhouse gas emission*
555 *pathways, in the context of strengthening the global response to the threat of climate*
556 *change, sustainable development, and efforts to eradicate poverty* (2018).
557 40. Yamaguchi, R. & Suga, T. Trend and Variability in Global Upper-Ocean
558 Stratification Since the 1960s. *J. Geophys. Res. Oceans* **124**, 8933–8948 (2019).

559 41. Gregory, J. M. *et al.* The Flux-Anomaly-Forced Model Intercomparison Project
560 (FAFMIP) contribution to CMIP6: investigation of sea-level and ocean climate change
561 in response to CO2 forcing. 27 (2016).
562 42. Todd, A. *et al.* Ocean-only FAFMIP: Understanding Regional Patterns of Ocean
563 Heat Content and Dynamic Sea Level Change. (2020).
564 43. Gille, S. T. Decadal-Scale Temperature Trends in the Southern Hemisphere
565 Ocean. *J. Clim.* **21**, 4749–4765 (2008).
566 44. Khatiwala, S. P. *et al.* Global ocean storage of anthropogenic carbon.
567 *Biogeosciences* **10**, 2169–2191 (2013).
568 45. Frölicher, T. L. *et al.* Dominance of the Southern Ocean in Anthropogenic
569 Carbon and Heat Uptake in CMIP5 Models. *J. Clim.* **28**, 862–886 (2015).
570 46. Roemmich, D. *et al.* Unabated planetary warming and its ocean structure since
571 2006. *Nat. Clim. Change* **5**, 240–245 (2015).
572 47. Durack, P. J., Gleckler, P. J., Landerer, F. W. & Taylor, K. E. Quantifying
573 underestimates of long-term upper-ocean warming. *Nat. Clim. Change* **4**, 999–1005
574 (2014).
575 48. McDougall, T. J. & Jackett, D. R. The material derivative of neutral density. *J.*
576 *Mar. Res.* **63**, 159–185 (2005).
577 49. Häkkinen, S., Rhines, P. B. & Worthen, D. L. Warming of the Global Ocean:
578 Spatial Structure and Water-Mass Trends. *J. Clim.* **29**, 4949–4963 (2016).
579 50. Desbruyères, D., McDonagh, E. L., King, B. A. & Thierry, V. Global and Full-
580 Depth Ocean Temperature Trends during the Early Twenty-First Century from Argo
581 and Repeat Hydrography. *J. Clim.* **30**, 1985–1997 (2017).
582 51. Iudicone, D. *et al.* Water masses as a unifying framework for understanding the
583 Southern Ocean Carbon Cycle. *Biogeosciences* **8**, 1031–1052 (2011).
584 52. Hawkins, E. *et al.* Uncertainties in the timing of unprecedented climates. *Nature*
585 **511**, E3–E5 (2014).
586

87 **[Figures]**

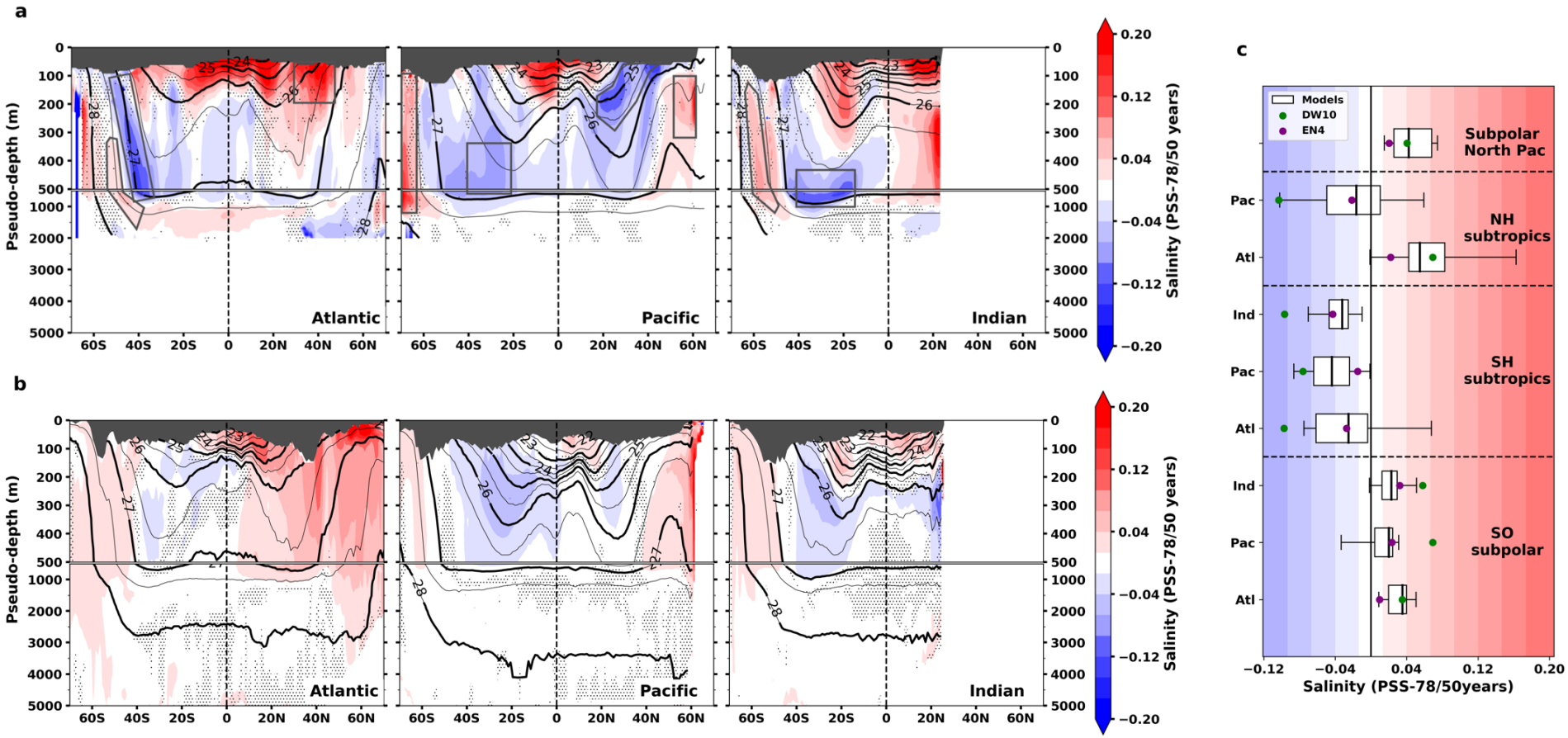

88

89 **Figure 1 Observed and simulated salinity changes between 1950 and 2008, shown in PSS-78/50 years, analysed on density surfaces**. For ease of
90 reading all figures of this paper are projected back from density to pressure as vertical coordinate (see Methods). (a) From Durack & Wijffels (2010)
91 observation-based analysis. Contours show isopycnals and stipples where the trend is not significant at the 90% confidence level. (b) From the multi-model
92 mean historical experiments. Contours show isopycnals and stipples indicate where less than 60% of models agree on the sign of the trend. The changes in
93 original density coordinate are shown in Supplementary Figure 1. (c) Trend averaged in 9 regions (approximate boxes shown in panel a) for 2 observational
94 estimates (Durack & Wijffels 2010 - DW10 - and EN4) and for the model distribution (boxes indicate 1st and 3rd quartiles and the median; whiskers indicate
95 the minimum and maximum outliers). The shading in (c) corresponds to the colour scale of (a) and (b). The exact regions in density space as used for each
96 observational dataset and model are plotted in Supplementary Figures 1a, 2a and 4 (same coordinates for both observational datasets). The greyed-out regions
97 at the surface correspond to data trimming above the bowl – see text.

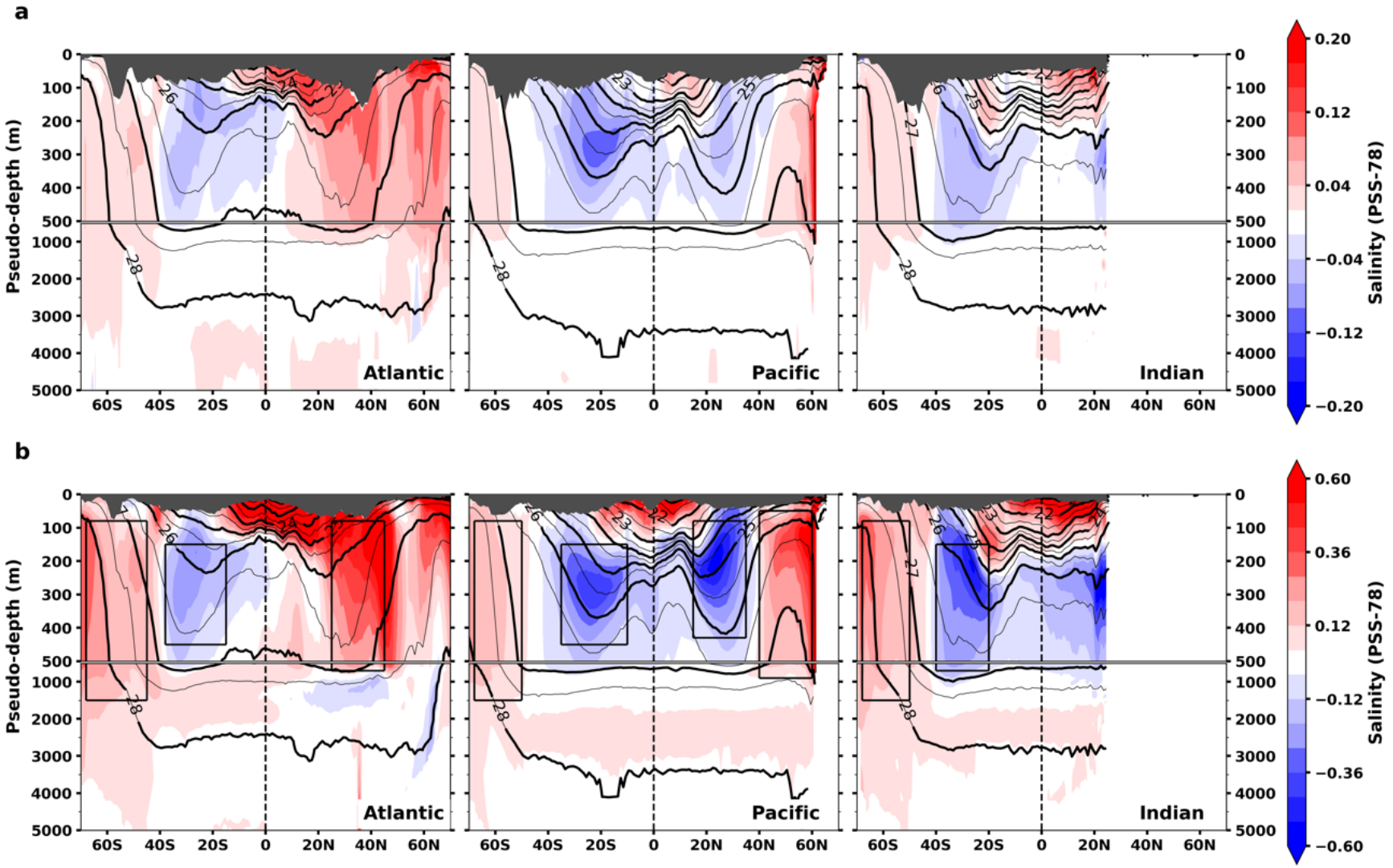

Figure 2 Anthropogenic salinity change along density surfaces. (a) At the end of the 20th century (multi-model mean difference between the last 20 years – to account for potential decadal variability – of the historical experiment and the historicalNat experiment). (b) At the end of the 21st century (multi-model mean difference between the last 20 years of the RCP8.5 scenario and the average of the whole historicalNat experiment). Boxes in (b) represent the approximate regions in which salinity trends are computed in Figure 1c and in which time of emergence is calculated in Figure 4. The same signal as in (b) is shown in Supplementary Figure 4 for each model in density space with the exact box locations.

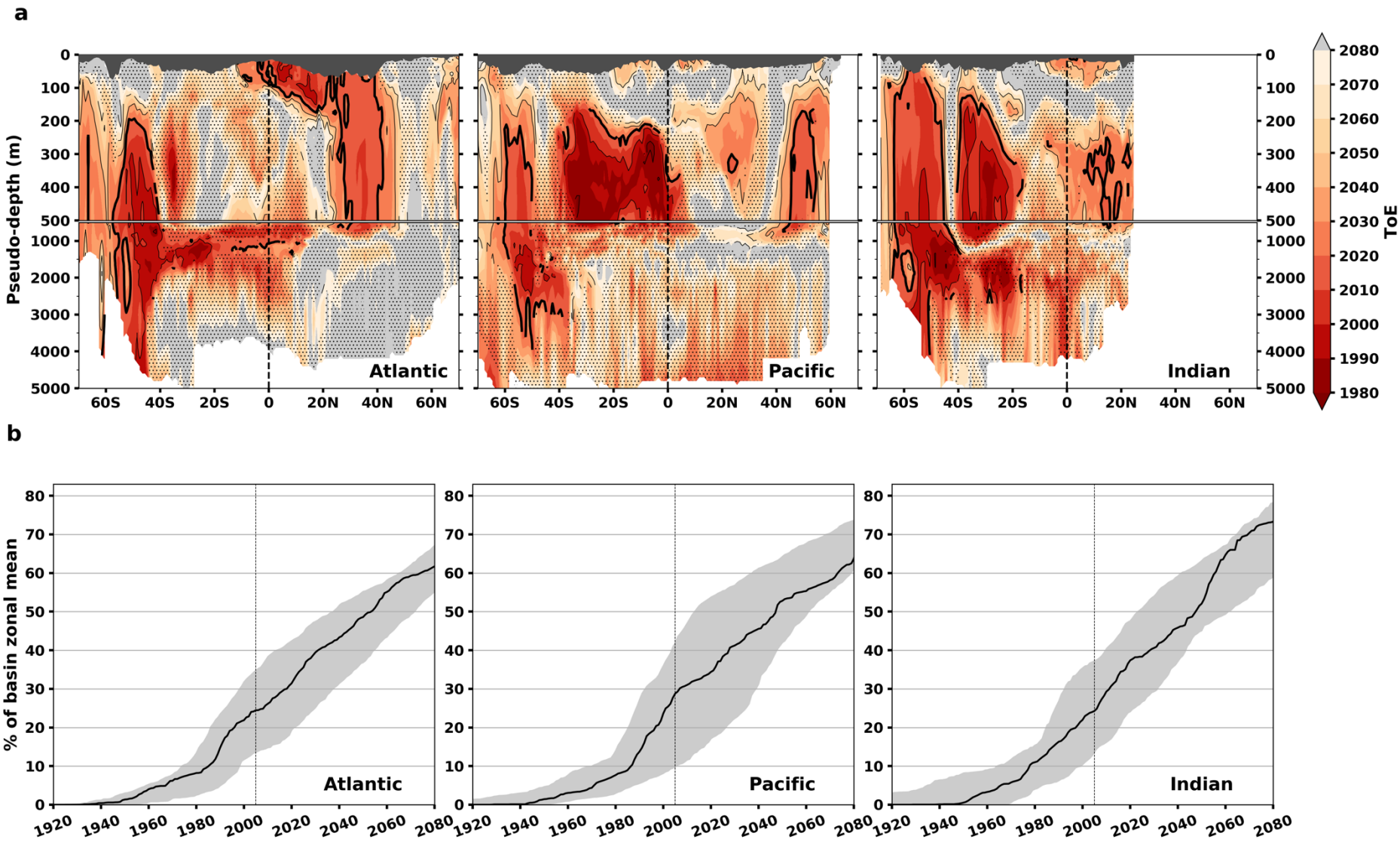

Figure 3 Time of emergence and percentage of emergence in basin zonal-means. (a) Multi-model median time of emergence of the anthropogenic salinity change, calculated for an ensemble of 11 models. Light grey regions mean no emergence of the signal, while stippled regions show where the models don't agree on the sign of the signal (see Methods). Bold contour is year 2020. (b) Percentage of basin emergence in zonal means under the bowl (see Methods). The black line is the median, the grey shading is the interquartile range.

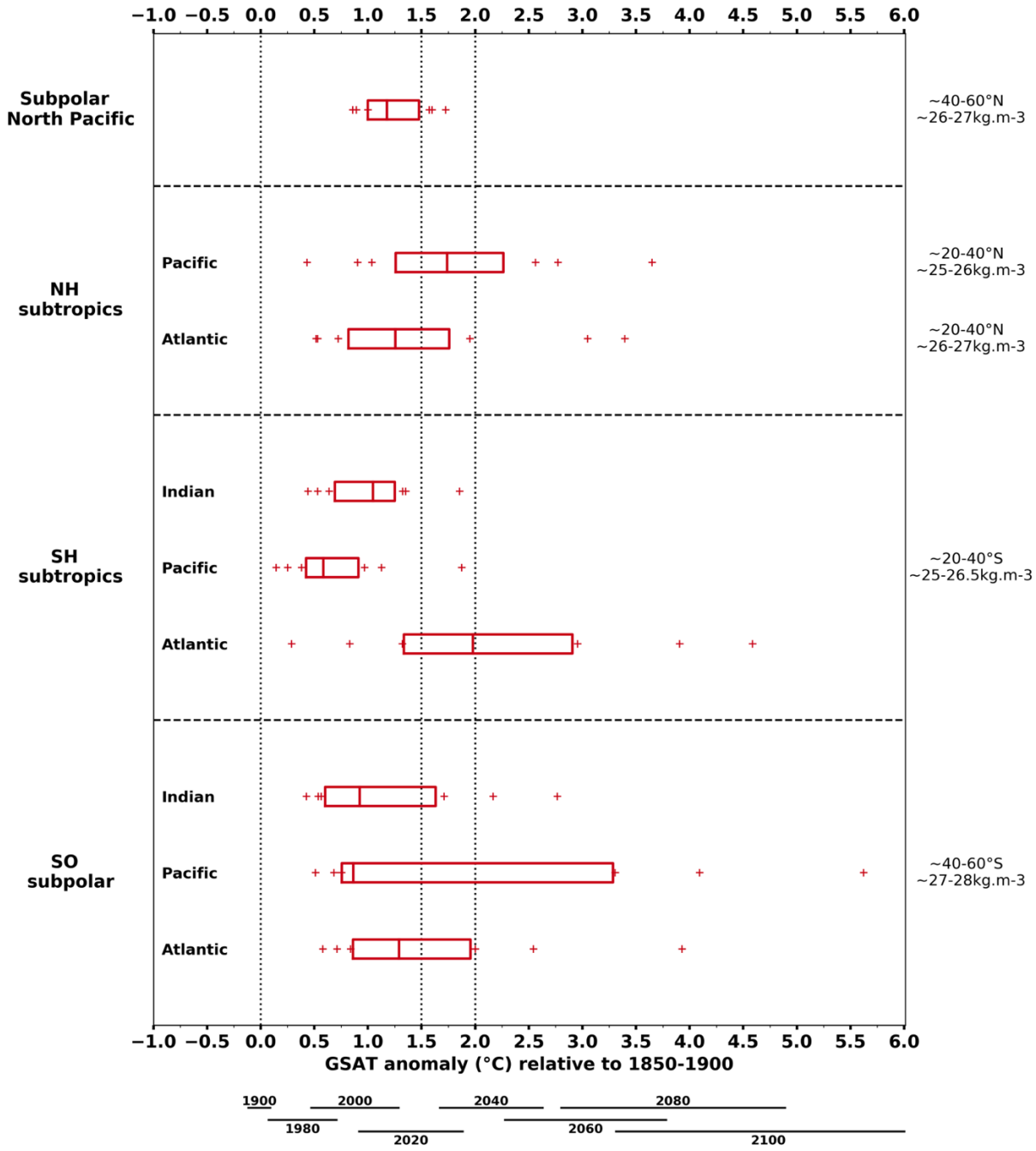

609

610 **Figure 4 Distribution of Global Surface Air Temperature at emergence**.
611 Calculated from the anthropogenic salinity signal and noise for each of the 11
612 models in 9 regions of interest: the Southern Ocean subpolar range, the Southern
613 Hemisphere subtropical range, the Northern Hemisphere subtropical range and the
614 subpolar North Pacific (the exact coordinates for each model are shown in
615 Supplementary Figure 4). Red boxes indicate 1st quartile, median and 3rd quartile.
616 A date reference was added below the warming axis, spanning the range of the
617 historical and RCP8.5 simulations.